Magnetic Resonance Imaging 61 (2019) 175–186

Contents lists available at ScienceDirect

Magnetic Resonance Imaging

journal homepage: www.elsevier.com/locate/mri

Original contribution

Non-contrast enhanced molecular characterization of C6 rat glioma tumor at 7 T

Mona Salehi Ravesh[a,b,*], Monika Huhndorf[b], Amir Moussavi[a,c]

[a] Section Biomedical Imaging, Molecular Imaging North Competence Center (MOIN CC), Department of Radiology and Neuroradiology, University Medical Center Schleswig-Holstein (UKSH), Kiel University, Kiel, Germany
[b] Department for Radiology and Neuroradiology, University Medical Center Schleswig-Holstein (UKSH), Kiel University, Kiel, Germany
[c] Functional Imaging Unit, German Primate Center, Leibnitz Institute for Primate Research, Göttingen, Germany

ARTICLE INFO

Keywords:
C6 rat glioma tumor
Non-contrast enhanced magnetic resonance imaging
Ultra high field
Chemical exchange saturation transfer (CEST)
Nuclear Overhauser Enhancement (NOE)
Magnetization transfer (MT)

ABSTRACT

Purpose: The aim of this study was to investigate, how to assess the relevant magnetization changes in the rat brain tissue due to the present of glioma tumor and its growth at a 7 T animal magnetic resonance imaging (MRI) system.
Material and methods: For this study, a custom-built two dimensional (2D) chemical exchange saturation transfer (CEST) pulse sequence was optimized for different tissue properties using fresh and cooked quail eggs. C6 tumor cells were investigated by *in-vivo* and *post-mortem* measurements in six Wistar rats using the optimized CEST sequence up to 5 weeks. Magnetization transfer ratio (MTR)- and asymmetric MTR (MTR_{asym})-maps of rat brains were created at different frequency offsets. *In-vivo* results were verified by ^1H spectroscopic, histological and also *in-vitro* C6 cell culture examinations.
Results: The CEST module for the optimal visualization of magnetization effects consists of five RF-pulses, each with a duration of 20 ms and a flip angle of 180°. *In-vivo* and *post-mortem* z-spectra of the cerebrospinal fluid (CSF), cortex, myelinated/demyelinated, healthy and tumorous tissue and tumor rim were obtained. The magnetization level and shape of the z-spectra on the upfield and downfield from the water peak were not the same. The magnetization dips on the upfield and downfield from the water peak of the z-spectra disappeared due to the thermal denaturation in cooked quail eggs and due to formaldehyde-induced fixation in *post-mortem* rat brains. The z-spectra of the rat brain in a range of ± 2 to ± 4 ppm displayed valuable information about the differentiation of various brain regions from the tumor tissue. Histological examinations confirmed our results. The C6 cell culture examinations showed that the observed magnetization changes in the rat brain occurred only due to the interaction between glioma cells and their environment in the rat brain and not from the C6 tumor cells.
Conclusions: Based on our *in-vivo* and *post-mortem* results, it is to be recommended to create the MTR-maps at a special offset frequency depending on the aim of research project instead of MTR_{asym}-maps. Otherwise, the desired effect attenuates or vanishes.

1. Introduction

Glioblastoma multiforme (GBM) is a highly aggressive brain cancer characterized by uncontrolled proliferation, resistance to cell death, extensive induction of angiogenesis, and vascular edema [1]. In the last decades, non-invasive magnetic resonance imaging (MRI) techniques have evolved into the most powerful and versatile imaging tool for brain tumor diagnosis, prognosis, therapy evaluation, monitoring of disease progression and planning of neurosurgical operations [2–5]. Generally, the MRI based diagnosis of glioblastoma in clinical routine is usually based on interpretation of signal intensity changes of ^1H protons in contrast enhanced (CE) spin-lattice (T_1)-weighted and spin-spin (T_2)-weighted MRI. Non-enhancing tumors can be detected using T_2-weighted MR imaging due to the prolonged T_2 relaxation time of hyperintense tumor tissue compare to surrounding healthy tissue [6]. CE T_1-weighted imaging shows a typically rim enhancing tumor with central necrosis representing only the macroscopic part of the tumor. Due to diffuse infiltration of Glioblastoma multiform even CE-MRI does not enable to differentiate vasogenic edema and microscopic tumor infiltration into surrounding tissue due to prolonged T_2 relaxation time

---

[*] Corresponding author at: University Medical Center Schleswig-Holstein (UKSH), Kiel University, Kiel, Arnold Heller, Street 3, Building 41, 24105 Kiel, Germany.
E-mail address: Mona.Salehiravesh@uksh.de (M. Salehi Ravesh).

https://doi.org/10.1016/j.mri.2019.05.036
Received 1 March 2019; Received in revised form 8 May 2019; Accepted 26 May 2019
0730-725X/

in both cases. Histologic studies showed tumor cell infiltration in T_2 hyperintense, non-contrast enhancing peritumoral regions and even further [7–9]. Visualization of these invading diffuse parts requires MR techniques that detect microscopic and functional changes such as ^{1}H-MR spectroscopy, as well as diffusion-weighted imaging (DTI) and perfusion. Moreover, although the long term clinical effect of the gadolinium based contrast agents are yet unknown, the interest for usage of contrast free MR techniques becomes even more important and necessary in clinical routine imaging, in particularly after the report of Kanda et al. in 2014 [10] about brain signal abnormalities after serial injection of gadolinium based contrast agents.

Chemical exchange saturation transfer (CEST) MRI [11] has recently emerged as an appropriate technique for molecular tumor research (tumor activity and tumor growth/size) [12]. The CEST technique is based on two ^{1}H proton pools in the tissue, a small pool of endogenous or exogenous exchangeable metabolite-bound ^{1}H protons and a large pool of ^{1}H protons in free bulk water. The bound ^{1}H protons resonate in a small chemical shift range of < 5 ppm beside the free water signal peak [13]. Applying radiofrequency presaturation pulses at appropriate frequency can saturate the exchangeable ^{1}H protons, which transfer from the metabolite pool into the free water pool by chemical exchange and thus reduce the equilibrium magnetization of the free water pool. The resulting CEST contrast on MR images depends on the amount of the exchanging magnetization through the chemical exchange between ^{1}H protons of metabolite pool and of free water pool. Therefore, the presence of specific chemical groups at very low concentration (μM to mM range [14]) in biological tissue can be measured indirectly through measurements of the signal intensity of free water protons (110 M) signal.

Amide proton transfer (APT) imaging was introduced [15,16] as a subgroup of CEST imaging, with that the exchange between protons of amide groups of endogenous mobile proteins and peptides and theirs of free water tissue is imaged. They demonstrated in a rat study with 9L gliosarcoma tumors [16] that APT-CEST imaging is able to distinguish between pathology-confirmed area of tumor and edema, which could not be accomplished using conventional MRI approaches, such as T_1-/T_2-weighted, in which the tumor boundaries appeared diffuse.

Recently, several research groups have observed an additional effect in a range of -2 to -5 ppm related to the water peak in the offset frequency-dependent z-magnetization (z-spectrum) [17–19]. As reported in previous studies, the observed Nuclear Overhauser Enhancement (NOE) effect in CEST experiments has been proposed in addition to APT as a potential new imaging contrast, which is sensitive to the concentration of mobile macromolecules, such as lipids, proteins, peptides in the tissue.

Some research groups [20–22] reported that glioma cell infiltration in white and grey matter (WM and GM) can be detected by determining of the macromolecular content of myelin using a variety of MR techniques based on magnetization transfer. In a human study at 7 T [23], it was shown that NOE signals are more sensitive than the conventional non-specific magnetization transfer (MT) to myelination.

The aim of this study was to investigate, how to assess the relevant magnetization changes for molecular characterization of rat brain tissue due to the presence of glioma tumor and its growth. This investigation was performed using *in-vivo*, *post-mortem* rat brain study, and also *in-vitro* examinations. A custom-built two dimensional (2D) CEST pulse sequence in this study was optimized for different tissue properties using fresh and cooked quail eggs. Following this, histological examinations were performed for the verification of the results from *in-vivo/post-mortem* rat studies.

2. Material and methods

2.1. CEST MRI acquisition

All MR imaging measurements were performed on a 7 Tesla horizontal bore small animal MR system (ClinScan, Bruker Biospin, Ettlingen, Germany) with a maximum gradient strength of 650 mT/m and a maximum slew rate of 1200 mT/m/ms using two radio frequency (RF) coils from Bruker. For *in-vivo* measurements: a volume resonator for RF excitation and a 4 channel rat surface coil (inner Ø = 3.0 cm) for signal reception were used. A transmit/receive volume coil (inner Ø = 3.8 cm) was used for *post-mortem* rat brain and *in-vitro* quail eggs measurements. Single-slice chemical exchange saturation transfer (CEST) pulse sequence was developed under Siemens IDEA environment for the syngo software version B15. The 2D CEST MR imaging was acquired in a range of -5 to 5 ppm using Gaussian-shaped RF saturation pulses followed by a Cartesian FLASH (Fast Low Angle SHot) readout. In addition, transverse magnetization was set to zero immediately before inter-pulse delay to represent the dephasing caused by crusher gradients, while its longitudinal magnetization relaxes towards its equilibrium state. The objects were located in the volume coils center and also close to the surface coil. Localized shimming (slice thickness 1 mm) was carried out for B_0 field homogenization. The temperature was kept at 37.0 ± 0.5 °C for *in-vivo* and fixed *post-mortem* rat brains, and at 21 ± 0.5 °C during the MR measurement of quail eggs. The measurement parameters are available in Table 1. A reference image in the absence of RF saturation (S_0) was also acquired for imaging signal intensity normalization. The z-spectra in quail eggs were acquired with a spectral resolution of 15 Hz and the z-spectra of rat brains and cell culture with 30 Hz.

2.2. Optimization of 2D CEST sequence

There are discrepancies between in previous studies reported/recommended parameter sets for small animal brain imaging by various field strengths [16,24–26]. The aim of the sequence optimization in our study was therefore to find out an optimal set of pulsed CEST sequence parameters for the detection of the (smallest) changes in magnetization transfer regarding to the glioblastoma tumor growth (*e.g.* over 5 weeks) at our 7 T animal MRI system. For detailed investigation the effect of variation of each sequence parameter on the detection of the changes in magnetization transfer, we separated the optimization procedure in 3 steps: 1) variation of RF pulse duration, 2) variation of FA, 3) variation of RF pulse iteration number. Fresh and cooked quail eggs were used as a biological phantom to mimic different brain tissue properties. For

Table 1
Protocol parameters for the cell culture, *in-vivo* and *post-mortem* rat brain measurements.

	FLASH								CEST		
	Slice orientation	FOV (mm^2)	Base resolution (Px)	Slice thickness (mm)	Band width (Hz/Px)	$FA_{\text{imaging module}}$ (°)	TR (ms)	TE (ms)	Pulse duration (ms)	Number of iteration	$FA_{\text{CEST module}}$ (°)
Cell culture	Tra	35 × 35	128 × 128	2	390	15	123	4.8	20	5	180
In-vivo/post-mortem				1							

FOV = field of view, Px = pixel, Hz = hertz, FA = flip angle, TE = echo time, TR = repetition time.

optimization measurements with quail eggs, each of these parameters was varied individually, while the other two remained constant.

2.2.1. RF pulse duration and flip angle

To investigate the influence of varying RF pulse duration on the shape of the measured z-spectra, fresh and cooked quail eggs were imaged with a common Gaussian-shaped RF pulse and various pulse duration of 10, 20, 40, 80, and 100 ms with an iteration number of 1 for representative CEST flip angle of 70°, 90°, 180°, 250°, 360° and 540°.

2.2.2. RF pulse iteration

For the investigation of the RF pulse iteration-dependent effect, the z-spectra were measured with a pulse iteration of 1, 5, 10, 20, and 40, using a common Gaussian-shaped pulse with a CEST flip angle of 70°, 90°, 180°, 250°, 360° and 540° and a duration of 10 ms. Additionally, z-spectra were measured with a RF pulse iteration number of 5 with the same flip angles and a pulse duration of 20 ms instead of 10 ms, which is still convenient for an *in-vivo* experiment from a temporal point of view.

2.3. Determination of T_1 and T_2 relaxation time

2D T_1- and T_2-weighted images of fresh and cooked quail eggs were acquired using gradient echo sequence and multi spin echo with the available parameters in Table 2. These images were used as a reference for the interpretation the influence of tissue properties on the CEST-effect in fresh and cooked Quail eggs. Additionally, the T_1 and T_2 relaxation time in two pure distilled water samples (Ultra Clear TM UV/UF, Siemens AG, PH = 7, total organic carbon < 1 ppb) were determined as a reference for the T_1 and T_2 on quail egg measurements.

The selected region of interest (ROI) for the z-spectra, T_1, T_2 measurements were located in the interested area of the object or in the middle of the phantom based on a sagittal oriented slice.

2.4. ^1H MR spectroscopy

Single-voxel ^1H magnetic resonance spectroscopy (MRS) with water suppression was performed at 300.24 MHz with a volume selective technique using the double spin echo (PRESS) under the same conditions in each experiment with the following parameters: repetition time (TR)/echo time (TE): 6000/10 ms, data points: 2048, RF excitation bandwidth: 200 kHz, voxel size. $2.5 \times 2.0 \times 1.0\ \text{mm}^3$, 128 averages, total measurement time: 13.1 min. The water peak at 4.7 ppm was referenced to Tetramethylsilane (TMS). MRS voxels were located in the interested area of the object or in the middle of the phantom based on a sagittal oriented slice.

2.5. Data analysis

Data processing was performed in Matlab (2017a, The Mathworks, Natick, MA, USA). Based on the computed B_0-inhomogeneities maps, a B_0-correction for the rats was not required, because the offset deviation was about ≤60 Hz from the minimum point of the z-spectrum at 0 ppm. The quantification of saturation transfer of the z-magnetization were illustrated using parameter maps, which were acquired pixel by pixel calculating the Magnetization transfer ratio:

$$\mathrm{MTR} = 100 \times [S_0 - S_{sat}(\pm\omega)]/S_0$$

$$\text{MTR asymmetry: } \mathrm{MTR_{asym}} = 100 \times [S_{sat}(-\omega) - S_{sat}(+\omega)]/S_0$$

at frequency offsets (ω) corresponding to the maximized intensity difference between the signal intensities from the ROIs in the tumor and healthy tissue. $S_{sat}(\pm\omega)$ and S_0 are the signal intensities with and without frequency selective excitation, respectively.

The spin-lattice relaxation time of water, T_1, was calculated using a three-parameter (A, α, TI) equation: $I = A \bullet \sin(\alpha)\frac{1 - e^{-TR/T_1}}{(1-\cos(\alpha)) \bullet e^{-TR/T_1}}$, where A, α, and TR are the initial Magnetization in z-direction, α the set flip angle, and the repetition times in the gradient echo sequence. The spin-spin relaxation time of water, T_2, was calculated using a three parameter equation (A, TE, B): $I = A \bullet e^{\frac{-TE}{T_2}} + B$ for the fitting the signal intensity-echo time-course, where A, TE, and B are the initial Magnetization in z-direction, the set echo times, and the offset constant between the basis line of Signal intensity-echo time (TE)-course and the TE axis.

The p-values for comparison of two groups were obtained from a Mann–Whitney U test as appropriate. A p-value < 0.05 was considered statistically significant. For statistical analysis, R Statistic package (Version 3.5.1, R Foundation for Statistical Computing, Vienna, Austria) was used.

2.6. Quail eggs

Fresh quail eggs (n = 4; mean weight: 14 ± 1 g, mean diameter: 9 ± 0.5 mm; mean height: 4 ± 0.5 mm) were used as biological phantom. Two of the eggs were cooked in 100 °C water for 10 min and cooled to room temperature of 21 °C for 2 h. Both fresh and cooked eggs were positioned in series in the receiver/transmitter volume coil to be measured simultaneously. The egg white consists of a gelatinous, semi-transparent liquid mixture containing about 10.4% proteins and 0.1% lipids [27]. The relatively solid egg yolk contains 49.8% water, 2.2% mineral substances, 16.6% proteins, 29.5% lipids, and 2% carbohydrates [28].

2.7. Tumor cell line

C6 glioma cell lines [29] are widely used in neuro-oncology for intracranial implantation in syngeneic Wistar rats. 100.000 rat glioma C6 cells were seeded one day before the MR experiment in a falcon tube with a volume of 20 ml and maintained in Dulbecco modified Eagle medium (DMEM, PAN Biotech, Aidenbach, Germany), which was supplemented with 10% fetal bovine serum (FBS, PAN Biotech, Aidenbach, Germany), 1% amphotericin B (PAN Biotech, Aidenbach, Germany), 1% penicillin and streptomycin (GIBCO Invitrogen, USA), and 4% L-glutamine (ROTH, Germany).

Table 2
Determination of theT_1 and T_2 relaxation times of quail eggs and distilled water.

Slice orientation	FOV (mm^2)	Base resolution (Px)	Slice thickness (mm)	Band width (Hz/Px)	FA (°)	TE (ms)	Number of averages	TR (ms)
sag	35 × 35	128 × 128	2	260	15	3.1	1	**T_1-measurements**: From 6 to 6000 with Several increments (> 20) depending on the measurement object
				130	180	From 11.9 to 381 ms in 32 increments		**T_2-measurements**: 6000

FOV = field of view, Px = pixel, Hz = hertz, FA = flip angle, TE = echo time, TR = repetition time.

2.8. Animal tumor model

Wistar rats ($n = 6$, male, mean weight = 333 ± 10 g, mean age = 6–10 weeks) were measured before the injection of tumor cells and once a week during 35 days after the injection. For the intracerebral injection of the tumor cells, the rats were anesthetized by intraperitoneal injection of 0.4 mg/kg medetomidine/70 mg/kg ketamine (10%). Through a small hole 3 mm left of the bregma a 5 μl suspension of C6 glioblastoma cells (100.000) were stereotactically injected into the left basal ganglia. For weekly follow up scans during the observation period, rats were anesthetized with intraperitoneal injection of 0.4 mg/kg medetomidine/70 mg/kg ketamine (10%) and intubated and ventilated to reduce moving artefacts and to sustain anesthesia with 1.5–2.0% isoflurane *via* endotracheal tube. The breathing rate was kept at 50 ± 5 breaths per minute monitored online through a small-animal monitoring and gating system connected with the respiration pneumatic sensor. Temperature was controlled by a rectal sensor and a tube system with circulating warm water. The rats were fixed to the surface coil in a supine position.

2.9. Fixation technique

After last MR measurement overdose of ketamine/xylazine was injected into the tail vain catheter. Thorax was opened and a cannula was inserted through the right ventricle into the ascending aorta. Then the left atrial auricle was opened by an incision. The rat was perfused by Phosphate-buffered saline (PBS) (PH = 7.0) until the liver turned pale pink, followed by perfusion of 4% paraformaldehyde, until the body was cataleptic. After perfusion the head was removed from the rest of the body and kept in a 4% paraformaldehyde solution for 48 h. After these 48 h another MRI examination of the fixed brain was performed.

2.10. Histology

After the *post-mortem* MRI measurements, the entire rat brain was extracted surgically from the rat head and dissected and sliced into two coronal sections from the middle of the tumor. These sections were placed for 48 h into 4% paraformaldehyde. After fixation paraffin fixation and paraffin embedding of the brain-sections, 7-μm slices were cut from each section using a microtome and then stained with hematoxylin and eosin, glial fibrillary acid protein (GFAP), von Willebrand factor (vWF) or luxol fast blue (LFB). GFAP is an intermediate filament protein that is expressed by numerous cell types of the central nervous system including astrocytes and ependymal cells during development. vWF is a blood glycoprotein involved in hemostasis. LFB is a commonly used stain to observe myelin under light microscopy. Presence of tumor and the pattern of infiltration were assessed and intrinsic tumor characteristics and effect of tumor presence on brain structure were recorded.

3. Results

3.1. Optimization of the 2D CEST MRI

The ^{1}H spectra of the fresh egg white and egg yolk with water suppression are shown in Fig. 1A and B. The peaks of egg whites ^{1}H spectra at 3.6, 3.3, 2.0, 1.3, and 0.9 ppm are very similar to those of proteins and nucleic acids. The peak at 4.7 ppm indicated the water peak in both ^{1}H spectra. In egg yolks ^{1}H spectra, from left side to right side the following peaks are detectable: 2.15 and 1.9 ppm: fatty acids such as linoleic, palmitic, and stearic acid, 1.2 ppm: CH_2 groups, and 0.8 ppm: CH_3 groups. The observation the effect of these peaks in measured z-spectra is used as a reference for the quality the optimization of sequence parameters.

The influence of varying the RF pulse duration on the shape of the measured z-spectra in the fresh egg white and egg yolk is displayed in Fig. 1C and D. Increasing the pulse duration from 10 to 40 ms leads to a significant reduction in the spectral width of the z-spectra by up to 1 ppm both in the fresh egg white and egg yolk. The spectral width of the z-spectra further decreases about < 0.25 ppm due to additionally increasing the pulse duration from 40 to 80 and 100 ms. The asymmetry between the right and left side of the z-spectra of fresh egg white and also the strength of their corresponding magnetization dips is strongly reduced due to increasing the pulse duration from 10 to 40 and furthermore to 100 ms (see frequency offset range of 1 to 4 and -1 to -4 ppm).

Generally, there is no magnetization (APT-CEST) dip in the downfield of the water peak in the z-spectra of fresh egg yolk (Fig. 1D). The asymmetry between the right and left side of the z-spectra is very strong due to the magnetization (NOE) dip in the upfield of the water peak. This asymmetry is significantly stronger than the observed one in the fresh egg white. By increasing the pulse duration from 10 to 100 ms, the depth and width of magnetization dip is reduced up to 10% and 0.5 ppm. As a consequence, the $(CH_2)_n$-peak gradually appears next to $(CH_3)_n$-peak.

The influence of the iteration number of RF Gaussian pulses on the shape of the measured z-spectra of the fresh and cooked egg white and egg yolk were investigated. The iteration number of RF pulse was increased from 1 to 5, 10, 20, and 40 with a constant RF pulse duration of 10 ms (Fig. 1E and F). A significantly asymmetry between the left and right side of z-spectra of the fresh and cooked egg white and egg yolk were appeared due to increasing the iteration number of RF pulse from 1 to 5. The asymmetric effect was negligible due to the increasing of the iteration numbers from 5 to 10, 20, and 40 times. In addition, the experiments were repeated with 5 iterations and a constant RF pulse duration of 20 ms. A combination of 5 iterations and a RF pulse duration of 20 ms led to achieve the maximum magnetization effect in fresh and cooked egg white and egg yolk, while the measurement time is not time consuming, *i.e.* for an *in-vivo* measurements (data not shown).

The influence of the variation of the flip angle of RF Gaussian pulse on the shape of the measured z-spectra of the fresh and cooked egg white (Fig. 1G and I) and fresh and cooked egg yolk (Fig. 1H and J) was investigated using five flip angles with a constant pulse duration of 20 ms and iteration number of 5. The increasing of the flip angle from 70° to 90°, 180°, 250°, 360° and 540° leads to a strongly increase the spectral width of the z-spectra both in the fresh and cooked egg white and egg yolk. This leads to a difference in the magnetization transfer level on the left and right side of the z-spectra, which is stronger in the fresh and cooked egg yolk compared to fresh and cooked egg white. The increasing of the flip angle from 70° to 180° and further to 250° leads to clearly appearance and also to increase the depth of magnetization dips in the fresh egg white and egg yolk. As a consequence of a further increasing the flip angle ($> 250°$) and its associated increasing the spectral width, the depth of magnetization dips are reduced in the fresh egg white and egg yolk.

In general, the asymmetry between the left and the right side of the z-spectra of the cooked egg white and egg yolk is reduced compared to fresh one. This reduction of asymmetry is stronger observable in the cooked white egg than the cooked egg yolk (Fig. 1I and J).

Thus, the optimized CEST module consists of five RF-pulses, each with a duration of 20 ms and a flip angle of 180° with the average B_1 of 0.10 μT [30].

3.2. T_1 and T_2 measurements

The measured T_1, T_2 of the fresh and cooked egg white and egg yolk, and also pure distilled water as a reference for these measurements are summarized in the Table 3.

3.3. Follow-ups of tumor growth

The follow up measurements in rat brains over 5 weeks were shown

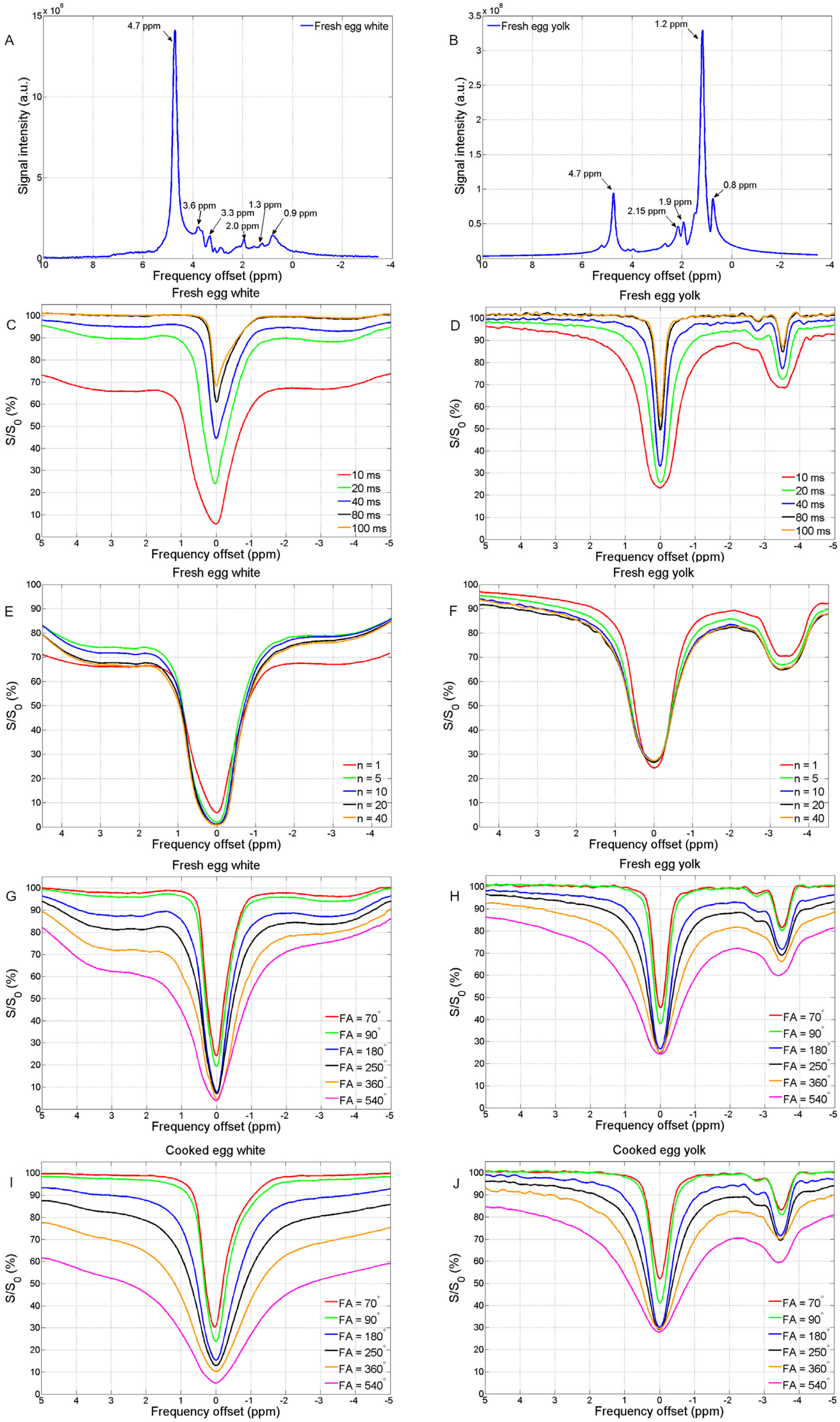

(caption on next page)

Fig. 1. A and B) ^{1}H spectra of fresh egg white and egg yolk with the water suppression. C and D) Z-spectra of fresh egg white and egg yolk with varying radio-frequency (RF) pulse duration. E and F) Z-spectra of fresh egg white and egg yolk with varying RF pulse iteration number. G–J) Z-spectra of fresh and cooked egg white and egg yolk with varying flip angle of the RF pulse. S and S_0 are the signal intensities with and without frequency selective excitation, respectively.

Table 3
T_1 and T_2 relaxation times of fresh, cooked quail eggs and pure water as a reference at 7 T animal MR system using two samples of each object. The values are given as mean ± standard deviation.

Measured object	T_2 (ms)	T_1 (ms)
Fresh quail egg		
Egg white	138.3 ± 6.8	792.0 ± 6
Egg yolk	25.7 ± 5.0	92.0 ± 6.1
Cooked quail egg		
Egg white	54.9 ± 2.4	703.1 ± 1.9
Egg yolk	21.7 ± 0.3	85.0 ± 10.2
Pure water	1063.4 ± 12.7	1509.7 ± 30.2

in Fig. 2. The images from left to right show the axial T_2-weighted images from the 0th day (before the injection) to the 35th day after the injection with 100.000 C6 glioma cells. The *in-vivo* measurements were performed based on this T_2-weighted images. The comparison between the images of the first, fifth and sixth rat show the continuously tumor growth during 5 weeks. Angiogenesis or necrotic regions are visible in brain tumors of rat number one, five and six on the 28th or 35th days after the injection of the tumor cells. In contrast to these, the tumor cells in the second, third and fourth rat did not grow well.

3.4. *In-vivo measurements*

The *in-vivo* axial T_2-weighted images of a rat brain tumor over 35 days after injection of C6 glioma tumor cells and the corresponding maps of MTR and MTR_{asym} at ± 3.5 ppm are shown in Fig. 3. The tumor growth is appeared over the weeks with a clear reduction of MTR and increasing of MTR_{asym}, which is in line with the T_2-weighted images. Both MTR and MTR_{asym} maps reflect the difference between the myelinated (orange arrow) and demyelinated (blue arrow) region caused by edema and tumor growth in the rat brain. The differentiation both between the tumor and healthy tissue and also between the myelinated and demyelinated region is even more pronounced on the MTR-maps at -3.5 ppm compared to the other two maps.

3.5. *Differentiation between different tissue types based on z-spectra and histological staining*

The normalized signal intensity from the ROIs in the cerebrospinal

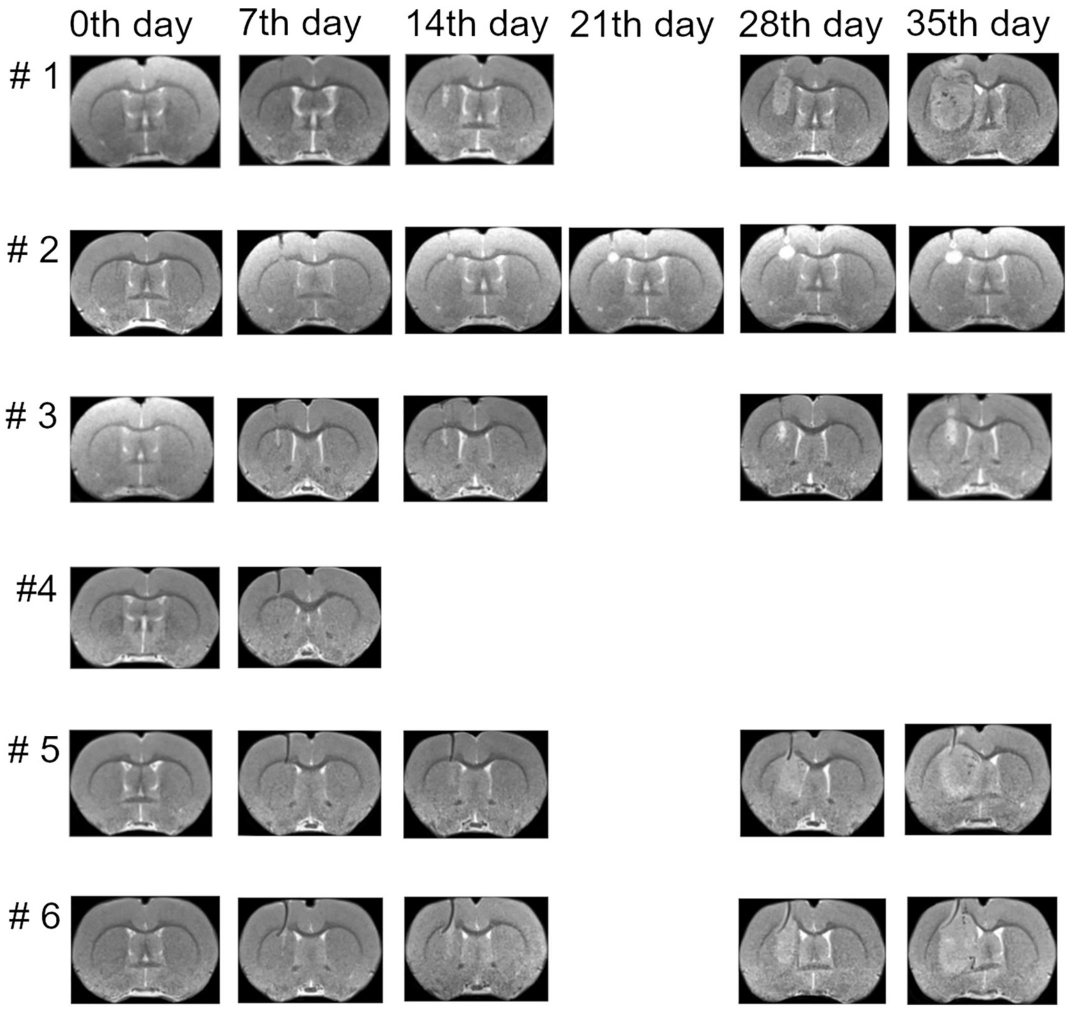

Fig. 2. *In-vivo* rat brain T_2-weighted MRI. The Follow-up measurements of rat brains with C6 tumor over 5 weeks from the day before the injection (day 0) and the last day of experiments. The rats were injected with 100.000 C6 cells. All rats were euthanized after the last measurement, but the rat number 4 died after the 7th day. Unfortunately, the rat number 3, 5, and 6 could not be examined on the 21th day due to urgent maintenance of the MRI system.

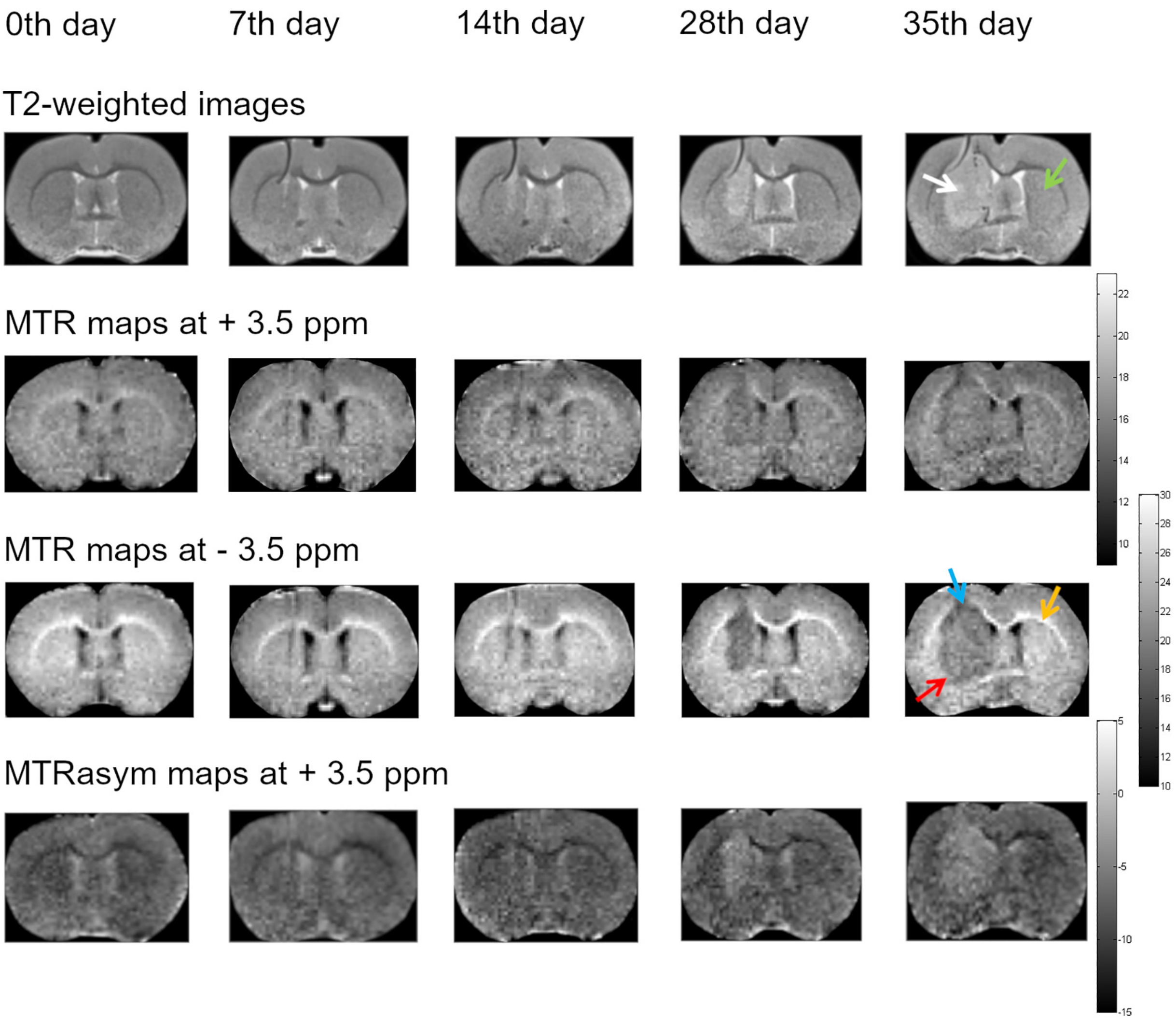

Fig. 3. *In-vivo* investigation of magnetization effect: Axial T_2-weighted brain glioma images of the rat no. 6 are displayed as anatomical reference for the MTR, and MTR_{asym} maps at ± 3.5 ppm over 35 days. The maps in each row are equally grey scaled. The white and green arrows point to tumor and normal brain tissue, the orange, blue, and red arrows show myelinated, unmyelinated region, and the tumor rim on images/maps, respectively. (For interpretation of the references to color in this figure legend, the reader is referred to the web version of this article.)

fluid (CSF), cortex, myelinated region, healthy and tumorous tissue, and tumor rim are displayed as a function of frequency offset in ppm (Fig. 4A). The measured z-spectra in the myelinated region shows the lowest magnetization level and that in CSF the highest both on the upfield and downfield from the water peak of z-spectrum compared to the measured z-spectra in other four regions. The magnetization levels of all six regions on the both sides of the z-spectra are not the same. This difference between the magnetization levels can be up to 10%, for instance in myelinated region. The z-spectra of CSF and of the myelinated region have the narrowest and widest spectral width. The z-spectra of cortex, healthy and tumorous tissue, and tumor rim are located between these spectra. All six z-spectra show clearly recognizable dips in a range of +2 to +4 ppm, and also −2 to −4 ppm. The depth of these dips are different. The z-spectra of cortex and the tumorous tissue overlap on the downfield, while their magnetization levels differ on the upfield from 5 to 10% in a range of 1.5 to 4.5 ppm.

Subfigures B, C, and D show three overview histological images with enlarged section of tumor rim, tumorous tissue and myelinated part in the rat brain, which stained using vWF to visualize vessels, GFAP to visualize reactive Astrocytes, and LFB method for visualization of myelinated fibers. The vWF staining shows tumor angiogenesis on the tumor rim in light brown and the tumorous cells in light violet. The GFAP staining shows a remarkable recruitment of astrocytes in the tumor rim in light brown. LFB staining enables to visualize myelinated fibers as in the corpus callosum stained light blue/turquoise, while tumor cells are stained deep violet.

3.6. *Investigation of the tumor growth over 35 days*

The changes of the normalized signal intensity from the ROIs in the tumor region and healthy tissue at ± 3.5 ppm are displayed in Fig. 5. Each data point at 0th and 35th day is a mean value of the corresponding data of rat number two, three, five, and six. The displayed error bars are the standard deviation of this data. A slight increase in the normalized signal intensity of the tumorous tissue between 0th and 35th day at +3.5 ppm can be observed. However, there is no significant difference between healthy and the tumor region ($p = 0.19$). At −3.5 ppm, the tumor region is differentiated from the healthy tissue due to increasing of its normalized signal intensity from 0th to 35th day ($p < 0.03$).

3.7. *Influence of denaturation on the tissue magnetization*

The normalized z-spectra of the *in-vivo* and *post-mortem* rat brain are shown as a function of frequency offset in Fig. 6A. The z-spectra of fresh and cooked white egg are displayed in Fig. 6B as a reference for fresh

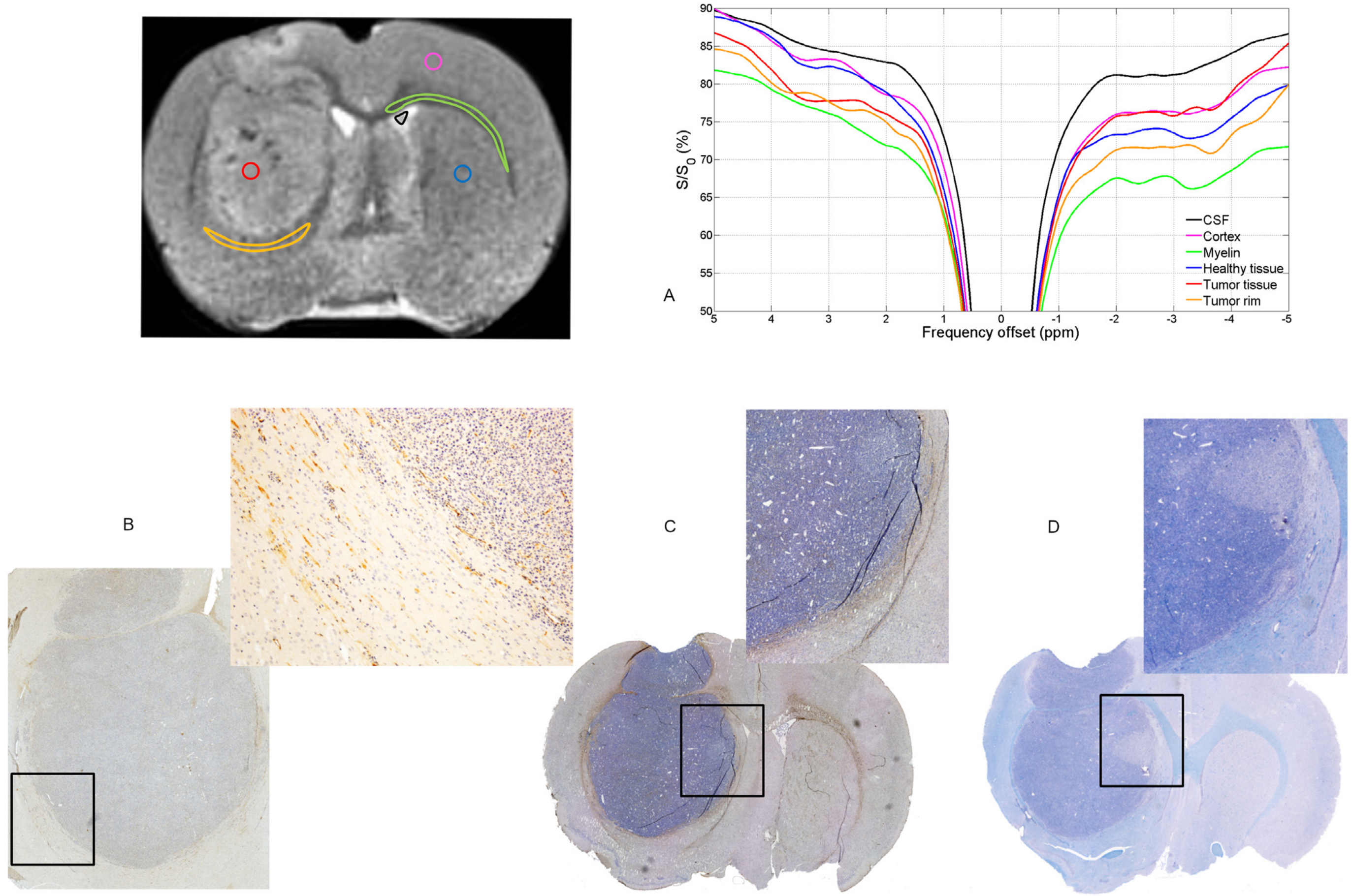

Fig. 4. Differentiation between different tissue types using CEST-MRI and histological staining. The selected ROIs for extraction the signal intensities from different brain parts of rat no. 1 and their z-spectra are shown in subfigure A. S and S_0 are the signal intensities with and without frequency selective excitation, respectively. Three overview histological images with enlarged section (black boxes) of tumor rim, tumorous tissue and myelinated part in the rat brain are displayed in subfigures B (von Willebrand factor, vWF), C (Glial fibrillary acidic protein, GFAP), and D (Luxol fast blue, LFB).

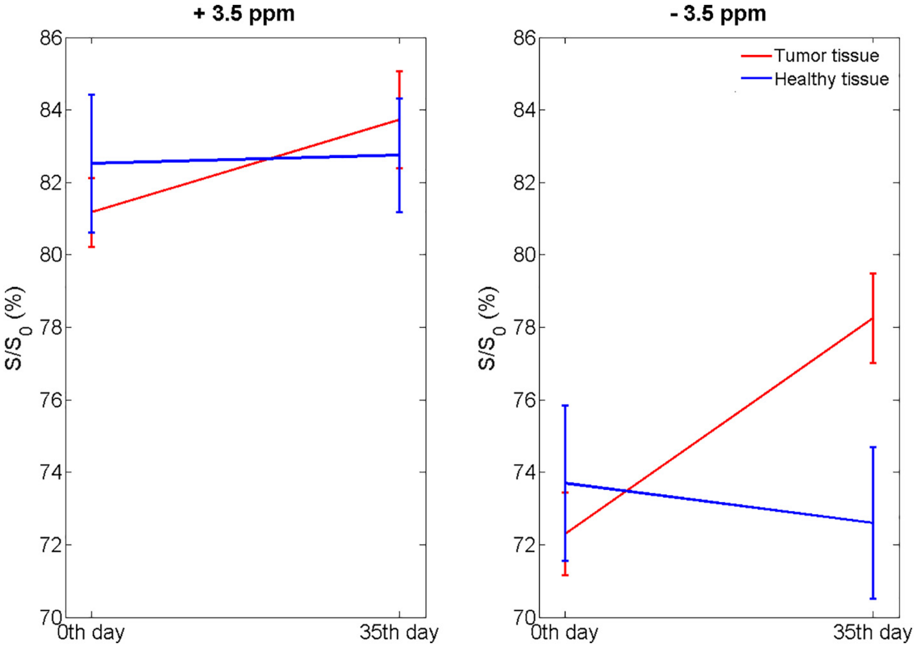

Fig. 5. Investigation of the tumor growth using magnetization effect. The changing the magnetization in the tumor region and healthy tissue at ± 3.5 ppm from 0th to 35th day is shown in subplots. S and S_0 are the signal intensities with and without frequency selective excitation, respectively.

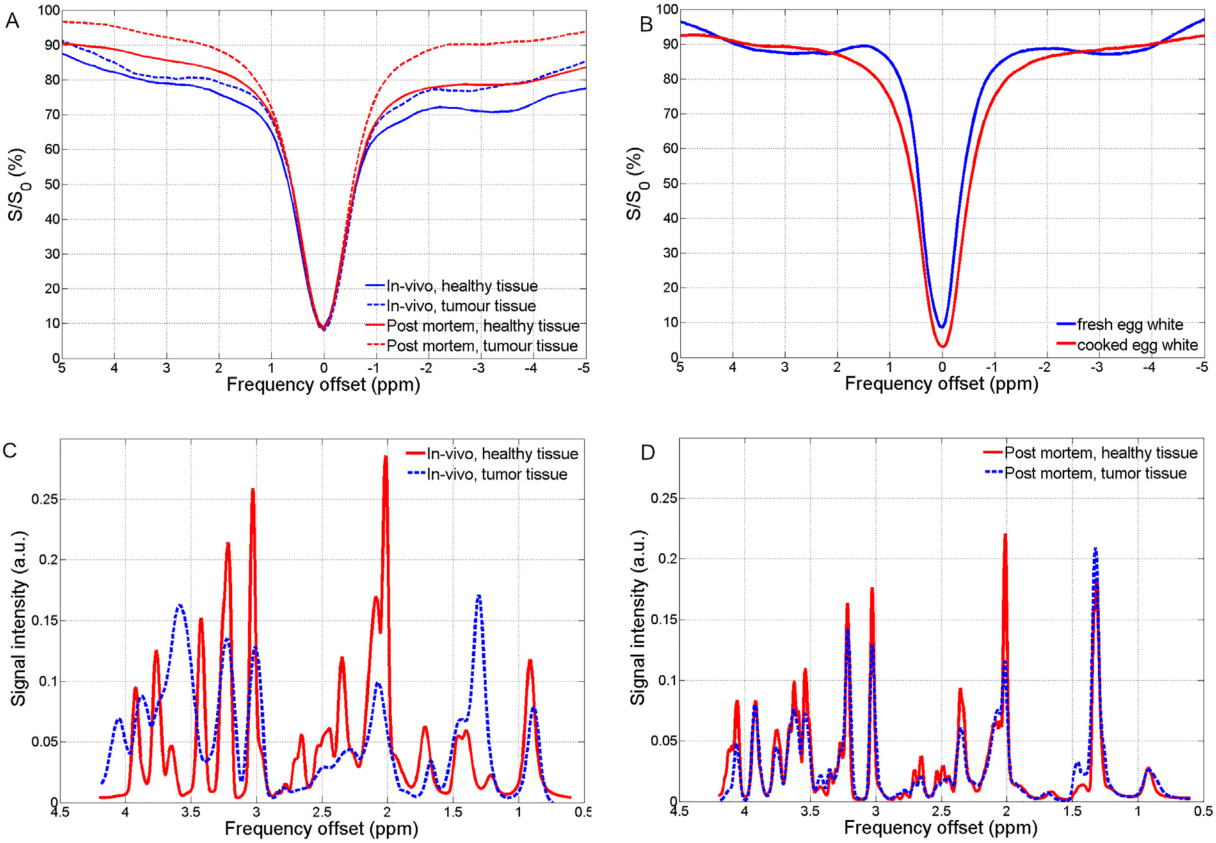

Fig. 6. Influence of denaturation on the magnetization effect. The normalized z-spectra of the *in-vivo* and *post-mortem* rat brain (no. 1), and fresh and cooked egg white as reference as a function of frequency offset (A, B). The corresponding ^{1}H-spectra of the *in-vivo* and *post-mortem* healthy and tumor tissues (C, D). S and S_0 are the signal intensities with and without frequency selective excitation, respectively.

(*in-vivo*) and fixed (*post-mortem*) cases.

There is a remarkable difference between the measured magnetization levels of the z-spectra in the tumorous and healthy tissue both in *in-vivo* and in *post-mortem* rat brains in an offset frequency range from ± 2 to ± 4 ppm. This difference is stronger on the upfield region of z-spectra (−2 to −4 ppm) compared with the downfield part (+2 to +4 ppm). The ratio of the magnetization levels between the healthy and tumorous tissue in *post-mortem* is about 3–5% higher than that in *in-vivo*. The observed dips of the z-spectra in the healthy and tumorous tissue of the *in-vivo* rat brain are disappeared in corresponding post-mortem z-spectra. The differences between the *in-vivo* and *post-mortem* z-spectra (concerning the disappearance of the magnetization dips) are in a good agreement with the showed differences between the fresh and cooked (denaturated) egg white (B).

The ^{1}H spectra of the *in-vivo* and *post-mortem* healthy tissue and the tumorous tissue are shown in Fig. 6C and D. The healthy tissue and tumorous tissue are indicated in red and dashed blue. From left to right there are the peaks of choline (3.2 ppm), creatine (3 ppm), NAA (2.1 ppm), and lactate (1.3 ppm) are detectable both in the *in-vivo* and in *post-mortem* healthy tissue and tumorous tissue. In generally, the ratio of choline to creatine peak changes between the healthy tissue and tumor tissue both in *in-vivo* and in *post-mortem* [31]. The NAA peak in healthy tissue is higher than in the tumor tissue both in *in-vivo* and in *post-mortem*. The lactate peak is elevated in tumor tissue than in the healthy tissue, but this difference is strongly reduced between the both tissues in *post-mortem*.

3.8. C6 cell culture

A with water-suppression measured ^{1}H-spectrum of a cell culture with 100.000 C6 glioma cells is shown in Fig. 7A. The normalized z-spectra of a cell culture with 100.000 C6 glioma cells is displayed in Fig. 7B (middle curve). Two samples filled with PBS and fresh quail egg white were measured simultaneously with the C6 cell culture as a reference for the cases without and with the strongest asymmetry between the right and the left side of the z-spectra. The frequency offset-dependent trend of the C6 z-spectra can be differentiated from the z-spectra of PBS in a range of −0.5 to −1.2 ppm and +0.25 to +2 ppm. Out of these ranges the shape of the z-spectra of the C6 cell culture is in a good agreement with that of the PBS. In contrast to the z-spectra of the fresh quail egg white, the z-spectra of the C6 cell culture doesn't show any dips neither on its right side nor on its left side. In order to investigate from which of the components of the cell culture this asymmetry comes from, the single component of the cell culture medium with the same used concentration in the cell culture were measured with the same parameter as in Fig. 7B. None of the z-spectra in Fig. 7C show a dip at the frequency offsets in a range of ± 2 to ± 5 ppm. The z-spectra of penicillin/streptomycin and Amphotericin B have the same shape like the PBS. The z-spectra of DMEM, FBS, and L-Glutamine show a similar frequency offset-dependent shape to the z-spectra of C6 cell culture. The asymmetry between the right and the left is demonstrated in the z-spectra of the DMEM and FBS. In order to figure out whether DMEM or FBS affects more the shape of the z-spectra of the C6 cell culture, the measurements were repeated using the same parameter set with three samples filled with pure DMEM, FBS, and a 50% mixture of both them (Fig. 7D). The comparison of C6 Z-spectra with the nutrient components' z-spectra indicates that the displayed asymmetry in the C6 Z-spectra is largely affected due to a mixture of DMEM and FBS.

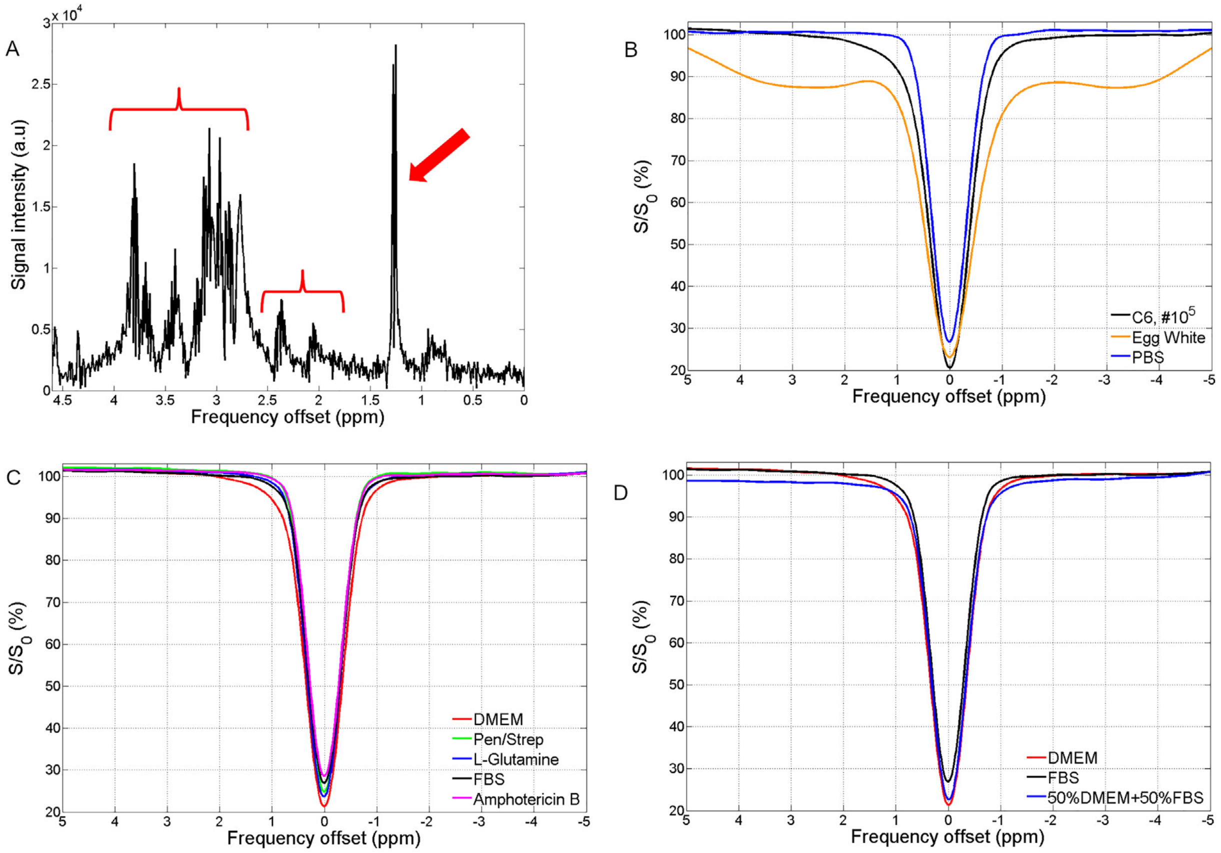

Fig. 7. C6 cell culture. A) ^{1}H MR spectrum of a cell culture with 100.000 C6 cells. B) z-spectra of C6 cell culture, PBS, fresh quail egg white, C) the components of nutrient solution and D) a composition of 50% DMEM and 50% FBS as a function of frequency offset in ppm. The red markings from left to right are assigned to DMEM, L-glutamine, and lactate. S and S_0 are the signal intensities with and without frequency selective excitation, respectively. (For interpretation of the references to color in this figure legend, the reader is referred to the web version of this article.)

4. Discussion

We investigated in this work the application of a non-contrast enhanced CEST MRI method for the early detection of magnetization changes in the rat brain tissue due to the presence of a glial tumor and its growth. In this study, we split our experiments in four parts: optimization of our custom-built 2D CEST pulse sequence, *in-vivo* and *post-mortem* imaging in a glioma rat model, histological examinations, and *in-vitro* C6 cell culture measurements.

Quail eggs were used as a biological phantom for the optimization experiments. Egg white and egg yolk have shown suitable for investigation the effect of the chemical structure of a tissue on the magnetization, because their chemical compositions are different in terms of protein and lipid content. The effect of the magnetization transfer rate and pH-value on the magnetization was investigated using fresh and cooked quail eggs.

Our first finding was that an “optimal” CEST-module consists of five RF-pulses, each of these has a duration of 20 ms and a flip angle of 180°. The optimization process can be improved with concurrently changing the parameter set based on multipool numerical simulations [30] or experimentally. The specific absorption rate (SAR) is proportional to the flip angle squared. We assume that we cannot use the same sequence design for human brain. The magnitude and duration of RF saturation pulse must be adjusted to the certain values, which do not exceed the SAR limit, but still provide a clinically diagnosable signal-to-noise ratio. In the literature, it is recommended to use lipid suppression in CEST sequence [32] to avoid the signal overlapping between the mobile macromolecule at -3.5 ppm with the signals due to the direct saturation of the large methylene peak of lipids.

In the second part of our study, 100.000 C6 Glioma cells were injected into the left basal ganglia of six male Wistar rates. The *in-vivo* measurements over 5 weeks after the injection of the tumor cells were performed once a week with the same parameter set. The z-spectra of CSF, cortex, myelin, healthy, tumorous tissue and tumor rim were compared together. The MTR- and MTR$_{asym}$-maps at different frequency offsets were created for the early detection of the tumor activity over 5 weeks. To verify our results, we performed detailed histological examinations of the rat brain samples with different staining methods (GFAP, vWF, and LFB). Gliomas as malignant primary brain tumors are characterized by extensive infiltration into the surrounding normal brain tissue [33]. There are two ways for dissemination of the tumor cells, along blood vessels [34] or along white matter fiber tracts, e. g. through the corpus callosum into the other hemisphere [33,35,36]. Myelin is an important component of the brain white matter. It contains both lipids (70–80%) and proteins (19–30%) [37] and surrounds the neural axons as a dielectric sheath. An *in-vivo* assessment of myelinated or demyelinated regions is beneficial for a comprehensive understanding of the involved mechanisms in brain tumor development and tumor cell migration [38].

Our second finding was that the z-spectra of CSF, cortex, myelin, healthy, tumorous tissue, and tumor rim have an asymmetric shape and the magnetization level are not the same on the upfield and downfield of their z-spectra. The lowest magnetization level belongs to myelin, the highest to CSF, and the other tissue types lie in between. The calculated MTR-maps at ± 3.5 ppm showed this asymmetry between the right and the left side of the z-spectra regarding to the contrast between the healthy tissue and tumor tissue, which is not negligible. Therefore, the differences between the magnetization transfer levels on the upfield and downfield of z-spectra cannot be taken into account, when the MTR$_{asym}$-maps calculate at different offset frequencies. The difference between the magnetization levels of the mentioned tissue types are higher on the upfield from the water peak compared to the downfield. This result and the position of the peaks in CSF, Myelin and cortex are in line with the presented z-spectra by Jin et al. at 9.4 Tesla in rat brains [39]. Therefore, the myelinated, healthy and tumorous tissue can be easily distinguished on a MTR-map at −3.5 ppm instead of on a MTR_{asym}-map on the same frequency offset.

Endogenous CEST contrast in the brain is always affected by intrinsic T_2, solid-like macromolecular MT and asymmetric mobile macromolecular (proteins, peptides, and lipids) MT effects based on the properties of the white and grey brain matter. Vavasour et al. [40] showed that macromolecular MT is not sensitive to myelin content due to the correlation between the water content and MTR contrast of myelin in presence of inflammation and edema, *e.g.* in multiple sclerosis brain. In contrast, the NOE-effect due to the changes in the concentration of mobile macromolecule is more sensitive to differentiation between myelinated and demyelinated regions [23]. The problem with the multi-contrast on the MTR_{asym}-map was described in several brain studies. Jin et al. [39] mentioned in their study that *in-vivo* quantitative mapping of APT-CEST-effect using the conventional asymmetry analysis is difficult due to the confounding NOE-effect and asymmetry of MT-effect from immobile macromolecules. Therefore, they obtained apparent maps for visualization of APT-CEST and NOE-effect. Paech et al. [41] calculated the maps for the visualization of the NOE-mediated CEST-effect in human brain at 7 Tesla at 3.3 instead of 3.5 ppm to avoid the influence of the APT-mediated effect that occurs at 3.5 ppm [42].

In the third part of our study, the influence of PFA as a fixation medium on the tissue properties and its magnetization transfer in the rat brain was investigated. With the usage of PFA, a reduced ^{1}H proton exchange rate in the rat brain tissue, comparable with the case of a tumor necrosis, could be simulated [43]. The T_1 and T_2 values of the fresh egg yolk about 700 ± 0.1 and 112 ± 1.8 ms are smaller than their corresponding values of the egg white. This difference is attributed to larger lipid content and smaller water content of egg yolk compared to the egg white [44]. The thermal denaturation leads to reduction of water content both in egg white and egg yolk and it appears in a significant decreasing of T_1 and T_2 values compared to these of fresh one. This results in the reduction of the asymmetry in the z-spectra of cooked egg white and egg yolk.

The differences between the z-spectra in *in-vivo* and *post-mortem*, and also in fresh and cooked egg white are based upon the different magnetization transfer rates between the corresponding tissue types due to the tissue denaturation. But, the mechanisms of the used denaturation methods for the rat brain and for the egg white are not the same. In cooked egg white, the presence of a thermal-induced cross-linking of macromolecules due to the heat-denaturation with possible increasing pH value [45] is responsible for the different magnetization transfer rate compared to the fresh egg white. In contrast, the formaldehyde-induced denaturation of rat brain tissue with perhaps pH differences between the *in-vivo* and *post-mortem* brain tissue led to disappearance of the magnetization dips in *post-mortem* z-spectra compared to the *in-vivo* z-spectra.

Our third finding was that asymmetric shape of the z-spectra in tumorous and healthy tissue disappeared due to the formaldehyde-induced denaturation, whereas the difference between their magnetization levels remains on the upfield and downfield from water peak on their z-spectra.

In the fourth part of our study, we investigated, whether the observed magnetization dips come originally from the C6 cells or occur due to the interaction of C6 glioma cells with the brain tissue cells. A preserved discrete chemical shift difference ($\Delta\ \omega$) between bulk water and the exchangeable proton on the solute site is the basic requirement of CEST contrast. For the selective saturation of the solute protons, the condition of slow exchange rate between water and solute pool ($k_{sw} \ll \Delta\ \omega$) has to be fulfilled. The saturation transfer efficiency in a CEST experiment is proportional to k_{sw}. At high exchange rate, the resonances of exchanging proton pools coalesce. Therefore, the CEST saturation pulse is not able to selectively saturate protons of solute pool without some direct saturation of bulk water pool. Thus, the CEST peak becomes broader [14], as demonstrated in the z-spectra of C6 cell culture. Our fourth finding based on the examinations with the C6 cell cultures was that the reported APT-CEST- and NOE-effects in glioma brain tumors [46] could not only be caused by glioma cells, but also be affected from the interaction between glioma cells and the tumor environment. The use of cell cultures as a biological phantom for tumor research projects can improve the investigation of specific targeted cells, and furthermore, can decrease the complexity of the experiments (e. g. lesser animal usage).

5. Conclusion

The z-spectra of the CSF, Cortex, myelinated/demyelinated, healthy and tumorous tissue at 7 Tesla field strength do not have the same magnetization level and same shape on the upfield and downfield of their z-spectra. Therefore, it is to be recommended to create the MTR-maps at a special offset frequency depending on the aim of research project instead of MTR_{asym}-maps. Otherwise, the desired effect attenuates or vanishes.

Acknowledgement

The authors thank Prof. Kirsten Hattermann-Koch, Judith Becker, Gabriele Trompke, and Kristin Kötz for the preparation of C6 Glioma Cells, histological examination and also for the technical support in MR measurements.

References

[1] Haskins WE, Zablotsky BL, Foret MR, Ihrie RA, Alvarez-Buylla A, Eisenman RN, et al. Molecular characteristics in MRI-classified group 1 glioblastoma multiforme. Front Oncol 2013;3:182.
[2] Gillies RJ, Bhujwalla ZM, Evelhoch J, Garwood M, Neeman M, Robinson SP, et al. Applications of magnetic resonance in model systems: tumor biology and physiology. Neoplasia 2000;2:139–51.
[3] Evelhoch JL, Gillies RJ, Karczmar GS, Koutcher JA, Maxwell RJ, Nalcioglu O, et al. Applications of magnetic resonance in model systems: cancer therapeutics. Neoplasia 2000;2:152–65.
[4] Pomper MG, Port JD. New techniques in MR imaging of brain tumors. Magn Reson Imaging Clin N Am 2000;8:691–713.
[5] Liu H, Hall WA, Martin AJ, Maxwell RE, Truwit CL. MR-guided and MR-monitored neurosurgical procedures at 1.5 T. J Comput Assist Tomogr 2000;24:909–18.
[6] Keunen O, Taxt T, Gruner R, Lund-Johansen M, Tonn J-C, Pavlin T, et al. Multimodal imaging of gliomas in the context of evolving cellular and molecular therapies. Adv Drug Deliv Rev 2014;76C:98–115.
[7] Watanabe M, Tanaka R, Takeda N. Magnetic resonance imaging and histopathology of cerebral gliomas. Neuroradiology 1992;34:463–9.
[8] Earnest 4th F, Kelly PJ, Scheithauer BW, Kall BA, Cascino TL, Ehman RL, et al. Cerebral astrocytomas: histopathologic correlation of MR and CT contrast enhancement with stereotactic biopsy. Radiology 1988;166:823–7.
[9] Scherer HJ. The forms of growth in gliomas and their practical significance. Brain 1940;63:1–35.
[10] Kanda T, Ishii K, Kawaguchi H, Kitajima K, Takenaka D. High signal intensity in the dentate nucleus and globus pallidus on unenhanced T1-weighted MR images: relationship with increasing cumulative dose of a gadolinium-based contrast material. Radiology 2014;270:834–41.
[11] Ward KM, Aletras AH, Balaban RS. A new class of contrast agents for MRI based on proton chemical exchange dependent saturation transfer (CEST). J Magn Reson 2000;143:79–87.
[12] Sakata A, Fushimi Y, Okada T, Arakawa Y, Kunieda T, Minamiguchi S, et al. Diagnostic performance between contrast enhancement, proton MR spectroscopy, and amide proton transfer imaging in patients with brain tumors. J Magn Reson Imaging 2017;46:732–9. https://doi.org/10.1002/jmri.25597.
[13] Zhou J, van Zijl PCM. Chemical exchange saturation transfer imaging and spectroscopy. Prog Nucl Magn Reson Spectrosc 2006:109–36.
[14] van Zijl Peter CM, Yadav NN. Chemical exchange saturation transfer (CEST): what is in a name and what isn't? Magn Reson Med 2011;65:927–48.
[15] Zhou J, Payen J-F, Wilson DA, Traystman RJ, van Zijl, Peter CM. Using the amide proton signals of intracellular proteins and peptides to detect pH effects in MRI. Nat Med 2003;9:1085–90.
[16] Zhou J, Lal B, Wilson DA, Laterra J, van Zijl, Peter CM. Amide proton transfer (APT)

contrast for imaging of brain tumors. Magn Reson Med 2003;50:1120–6.

[17] Jones CK, Huang A, Xu J, Edden Richard AE, Schär M, Hua J, et al. Nuclear Overhauser enhancement (NOE) imaging in the human brain at 7 T. Neuroimage 2013;77:114–24.

[18] Liu D, Zhou J, Xue R, Zuo Z, An J, Wang Danny JJ. Quantitative characterization of nuclear Overhauser enhancement and amide proton transfer effects in the human brain at 7 Tesla. Magn Reson Med 2013;70:1070–81.

[19] Zaiss M, Kunz P, Goerke S, Radbruch A, Bachert P. MR imaging of protein folding in vitro employing nuclear-Overhauser-mediated saturation transfer. NMR Biomed 2013;26:1815–22.

[20] Underhill HR, Rostomily RC, Mikheev AM, Yuan C, Yarnykh VL. Fast bound pool fraction imaging of the in vivo rat brain: association with myelin content and validation in the C6 glioma model. NeuroImage 2011;54:2052–65.

[21] Trozer DJ, Benton CD, Cercignani M, Tofts PS, Rees JH. Quantitative magnetization transfer parameters show dramatic changes in low grade gliomas. Proceedings of the 15thA annual Mmeeting of ISMRM, Berlin, Germany. 2007. p. 2852.

[22] Garcia M, Gloor M, Stippich C, Jax F, Scheffler K, Bieri O. Anylysis of brain tumors and metastases by quantitative MT imaging with bSSFP: Initial experinces. Proceedings of the 18th Aannual Mmeeting of ISMRM, Stockholm, Sweden. 2010. p. 2176.

[23] Mougin O, Clemence M, Peters A, Pitiot A, Gowland P. High-resolution imaging of magnetisation transfer and nuclear Overhauser effect in the human visual cortex at 7 T. NMR Biomed 2013;26:1508–17.

[24] Xu J, Zaiss M, Zu Z, Li H, Xie J, Gochberg DF, et al. On the origins of chemical exchange saturation transfer (CEST) contrast in tumors at 9.4 T. NMR Biomed 2014:406–16.

[25] Sagiyama K, Mashimo T, Togao O, Vemireddy V, Hatanpaa KJ, Maher EA, et al. In vivo chemical exchange saturation transfer imaging allows early detection of a therapeutic response in glioblastoma. Proc Natl Acad Sci U S A 2014;111:4542–7.

[26] Salhotra A, Lal B, Laterra J, Sun PZ, van Zijl, Peter CM, et al. Amide proton transfer imaging of 9L gliosarcoma and human glioblastoma xenografts. NMR Biomed 2008;21:489–97.

[27] Dudusola IO. Comparative evaluation of internal and external qualities of eggs from quail and guinea fowl. Int Res J Plant Sci 2010:112–5.

[28] Prelipcean (Teuşan) A, Prelipcean AA, Teuşan V. Investigation on the structure, chemical composition and caloricity of the quail eggs, deposited at the plateau phase of the laying period. Lucrari Stiintifice–Seria Zootehnie. 2012.

[29] Benda P, Lightbody J, Sato G, Levine L, Sweet W. Differentiated rat glial cell strain in tissue culture. Science 1968;161:370–1.

[30] Zu Z, Li K, Janve VA, Does MD, Gochberg DF. Optimizing pulsed-chemical exchange saturation transfer imaging sequences. Magn Reson Med 2011;66:1100–8.

[31] Horska A, Barker PB. Imaging of brain tumors: MR spectroscopy and metabolic imaging. Neuroimaging Clin N Am 2010;20:293–310.

[32] Lu J, Zhou J, Cai C, Cai S, Chen Z. Observation of true and pseudo NOE signals using CEST-MRI and CEST-MRS sequences with and without lipid suppression. Magn Reson Med 2015;73:1615–22.

[33] Russell DS, Rubinstein LJ. Pathology of tumours of the nervous system. 5th ed. London: Arnold; 1989.

[34] Giese A, Loo MA, Tran N, Haskett D, Coons SW, Berens ME. Dichotomy of astrocytoma migration and proliferation. Int J Cancer 1996;67:275–82.

[35] Burger PC, Heinz ER, Shibata T, Kleihues P. Topographic anatomy and CT correlations in the untreated glioblastoma multiforme. J Neurosurg 1988;68:698–704.

[36] Pedersen PH, Edvardsen K, Garcia-Cabrera I, Mahesparan R, Thorsen J, Mathisen B, et al. Migratory patterns of lac-z transfected human glioma cells in the rat brain. Int J Cancer 1995;62:767–71.

[37] O'Brien JS, Sampson EL. Lipid composition of the normal human brain: gray matter, white matter, and myelin. J Lipid Res 1965;6:537–44.

[38] Amberger VR, Hensel T, Ogata N, Schwab ME. Spreading and migration of human glioma and rat C6 cells on central nervous system myelin in vitro is correlated with tumor malignancy and involves a metalloproteolytic activity. Cancer Res 1998;58:149–58.

[39] Jin T, Wang P, Zong X, Kim S-G. MR imaging of the amide-proton transfer effect and the pH-insensitive nuclear Overhauser effect at 9.4 T. Magn Reson Med 2013;69:760–70.

[40] Vavasour IM, Laule C, Li DKB, Traboulsee AL, MacKay AL. Is the magnetization transfer ratio a marker for myelin in multiple sclerosis? J Magn Reson Imaging 2011;33:713–8.

[41] Paech D, Zaiss M, Meissner J-E, Windschuh J, Wiestler B, Bachert P, et al. Nuclear Overhauser enhancement mediated chemical exchange saturation transfer imaging at 7 Tesla in glioblastoma patients. PLoS One 2014;9:e104181.

[42] Zhou J, Blakeley JO, Hua J, Kim M, Laterra J, Pomper MG, et al. Practical data acquisition method for human brain tumor amide proton transfer (APT) imaging. Magn Reson Med 2008;60:842–9.

[43] Mehrabian H, Desmond KL, Soliman H, Sahgal A, Stanisz GJ. Differentiation between radiation necrosis and tumor progression using chemical exchange saturation transfer. Clin Cancer Res 2017;23:3667–75.

[44] Zhou J, Yan K, Zhu H. A simple model for understanding the origin of the amide proton transfer MRI signal in tissue. Appl Magn Reson 2012;42:393–402.

[45] Hee Lee M, Jung C, Sik Choi E, Sohn S. The effect of storage period and temperature on egg quality in commercial eggs. Kor J Poult Sci 2016;43.

[46] Zhou J, Hong X, Zhao X, Gao J-H, Yuan J. APT-weighted and NOE-weighted image contrasts in glioma with different RF saturation powers based on magnetization transfer ratio asymmetry analyses. Magn Reson Med 2013;70:320–7.